Original Article

INDONESIAN JOURNAL OF NATURAL PRODUCTS CHEMISTRY

Exploration of an Ancient Dye: Synthesis and Modeling an Indirubin-Inspired GSK-3β Inhibitor

Muhammad Naufal[1], Ade Danova[2], Elvira Hermawati[2], Ika Wiani Hidayat[1], and Jamaludin Al-Anshori[1*]

[1]*Department of Chemistry, Faculty of Mathematics and Natural Sciences, Universitas Padjadjaran, Jatinangor 45363, Indonesia.*

[2]*Organic Chemistry Division, Faculty of Mathematics and Natural Sciences, Bandung Institute of Technology, Jl.Ganesha 10, Bandung, West Java, 40132, Indonesia.*

*Corresponding author's: jamaludin.al.anshori@unpad.ac.id

Abstract

Indirubin, a bis-indole alkaloid found in indigo-producing plants and Indigo Naturalis, exhibits a broad range of pharmacological activities and serves as a versatile scaffold for medicinal chemistry modification. In this study, 5-(2-oxoindolin-3-ylidene)imidazolidine-2,4-dione (**4**) was synthesized via Knoevenagel condensation of isatin and hydantoin under acetic acid reflux with sodium acetate catalysis, affording the product in 44% yield. The structure was confirmed by ^{1}H-NMR, ^{13}C-NMR, and high-resolution ESI-TOF mass spectrometry. Density functional theory (DFT) calculations at the B3LYP-D4/def2-SVP level revealed a HOMO–LUMO gap of 3.27 eV, indicating moderate electronic stability alongside appreciable electron-accepting character, further supported by the calculated global reactivity descriptors. Electron localization function (ELF) and localized orbital locator (LOL) analyses indicated coexisting localized heteroatom lone-pair density and delocalized π-electron character across the conjugated framework. Molecular docking against GSK-3β showed that compound **4** occupies the ATP-binding site and reproduces key hinge hydrogen-bond interactions through its indole moiety. This combined synthetic, electronic, and docking results identify compound **4** as a promising indirubin-derived scaffold for further development as a GSK-3β inhibitor.

Keywords: indirubin, Knoevenagel condensation, DFT, GSK-3β, molecular docking.

INTRODUCTION

Indirubin (Figure 1) is a naturally occurring bis-indole alkaloid that has been identified primarily in indigo-producing plants, including *Baphicacanthus cusia*, *Polygonum tinctorium*, *Isatis indigotica*, *Isatis tinctoria*, *Strobilanthes cusia*, and *Indigofera tinctoria* [1–5]. Indirubin is also recognized as one of the bioactive constituents of *Indigo Naturalis* (Qingdai), a traditional blue-powdered Chinese medicinal preparation. Increasing pharmacological evidence has demonstrated that indirubin and its derivatives possess a broad spectrum of biological activities, including anticancer, anti-inflammatory, neuroprotective, anticonvulsant, and antimicrobial effects [6–9].

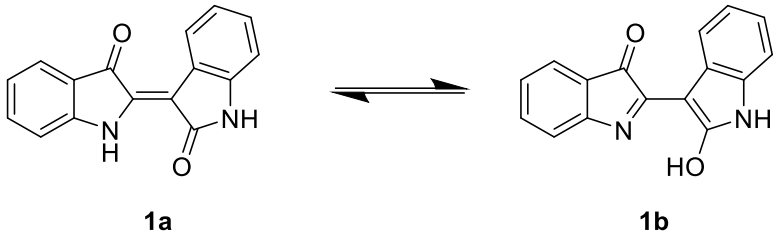

1a **1b**

Figure 1. Structure of indirubin.

From a chemical and medicinal chemistry standpoint, the indirubin scaffold offers a versatile platform for molecular modification, since substitution on the indole rings can alter its physicochemical characteristics, electronic structure, and biological activity. The pioneering work of Hill and Henze demonstrated the synthesis of an indirubin analogue via Knoevenagel condensation of isatin with hydantoin, employing sodium acetate as a catalyst in acetic acid [10]. This approach was subsequently extended to related heterocyclic systems, with isatin undergoing condensation with thiohydantoin, rhodanine, and thiazolidine derivatives to afford structurally diverse indirubin analogues [6,11–15]. In view of the chemical and biological relevance of these compounds, the present study aims to synthesize indirubin derivatives and systematically examine their physicochemical, electronic, and molecular properties.

EXPERIMENTAL SECTION

Material and Instrumental

All chemicals were acquired from commercial suppliers (Sigma Aldrich, TCI) and used without additional purification. All solvents were sourced from non-commercial sources and subsequently purified by distillation for further use. Thin-layer chromatography (TLC) was conducted on Merck TLC plates (0.23 mm thickness) and visualized using UV light. NMR measurements were performed using an Agilent Varian DD2 500 MHz spectrometer. Mass spectra (MS) were obtained using a Waters LCT Premier XE ESI-TOF-MS.

Methods

Synthesis of 5-(2-oxoindolin-3-ylidene)imidazolidine-2,4-dione (**4**). Isatin (**2**) 1.1 mmol, hydantoin (**3**) 1 mmol, and sodium acetate 1 mmol were dissolved in 1 mL of acetic acid under reflux condition for 16 hours. The reaction was monitored with thin layer chromatography (TLC). Upon completion, reaction was quenched using cold water and washed with ethanol. 100 mg of Brown solid product was obtained with yield of 44% ^{1}H-NMR (500 MHz, DMSO-d_6) δ 11.80 (s, 1H), 10.89 (s, 1H), 10.44 (s, 1H), 8.49 (d, J = 7.7 Hz, 1H), 7.24 (t, J = 7.6 Hz, 1H), 7.00 (t, J = 7.7 Hz, 1H), 6.89 (d, J = 7.7 Hz, 1H). ^{13}C-NMR (126 MHz, DMSO-d_6) δ 169.59, 164.88, 154.11, 141.48, 134.26, 129.64, 125.33, 121.54, 120.31, 109.87, 107.26, 39.52. HR-ESI-TOF-MS m/z: $[M-H]^-$ 228.0415 (calculated $[M-H]^-$ $C_{11}H_6N_3O_3^-$ 228.0409).

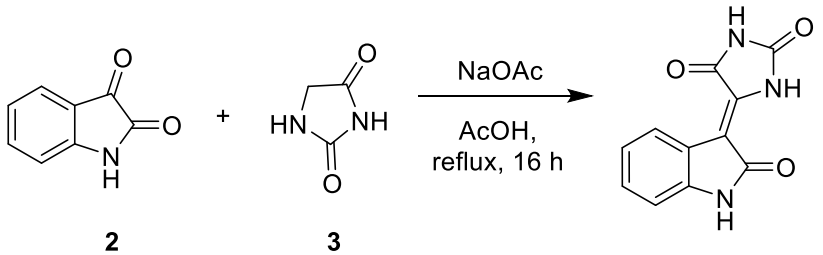

2 **3** **4**, 44%

Figure 2. Synthesis route of 5-(2-oxoindolin-3-ylidene)imidazolidine-2,4-dione.

Frontier Molecular Orbital analysis. Density functional theory (DFT) calculations were performed using ORCA 6.1 to investigate the electronic properties of the synthesized compounds [16]. Prior to electronic structure calculations, the molecular geometries were fully optimized without any symmetry constraints at the B3LYP-D4/def2-svp theory level. The optimized geometries were subsequently used for FMO analysis without further structural modification [17]. Based on Koopman's theorem, several global reactivity descriptors were calculated from the HOMO and LUMO energies. The ionization energy (IP) and electron affinity (EA) were estimated as $IP \approx -E_{\mathrm{HOMO}}$ and $EA \approx -E_{\mathrm{LUMO}}$, respectively. The HOMO-LUMO energy gap (ΔE), chemical hardness (η), electronegativity (χ), chemical potential (μ), and electrophilicity index (ω) were subsequently calculated according to the following equations:

$$\Delta E = E_{\mathrm{LUMO}} - E_{\mathrm{HOMO}}$$

$$\eta = \frac{IP - EA}{2}$$

$$\chi = \frac{IP + EA}{2}$$

$$\mu = \frac{(IP + EA)}{2}$$

$$\omega = \frac{\mu^2}{2\eta}$$

These descriptors were employed to evaluate the electronic stability, electron donating and electron-accepting capabilities, and the overall chemical reactivity of the investigated compounds. In addition, ELF and LOL were analyzed using Multiwfn 2026 [18].

Molecular docking. The crystal structure of GSK-3β in complex with a co-crystallized ligand was obtained from the Protein Data Bank (PDB ID: 1Q41) [19]. The protein structure was prepared prior to docking by removing non-essential residues and the co-crystallized ligand, followed by addition of hydrogen atoms and assignment of appropriate partial charges. The prepared receptor was subsequently converted to PDBQT format for docking calculations [20]. The synthesized compounds geometries were obtained from DFT calculation. Docking calculations were performed using AutoDock Vina 1.2.7 [21]. The binding site and the grid box were defined and cantered on the position of the co-crystallized ligand in the GSK-3β crystal structure. The resulting protein-ligand interactions were subsequently analyzed and visualized using ChimeraX and PoseEdit available through the ProteinPlus web server [22].

RESULTS AND DISCUSSION

The synthesized compound **4** were characterized using ^{1}H-NMR, ^{13}C-NMR, and high-resolution mass spectrometry. In ^{1}H-NMR spectrum (Figure 3), the amide protons appeared in the range of 10.44–11.80 ppm, with the N-3 proton exhibiting the greatest downfield shift. This pronounced deshielding is attributed to the formation of an intermolecular hydrogen bond between the N-3 proton and the carbonyl oxygen at C-2. The aromatic proton signals were observed over the range of 6.88–8.50 ppm. The doublet signals were assigned to H-4 and H-7, whereas the triplet signals corresponded to H-5 and H-6. In ^{13}C-NMR spectrum, the vinylidene carbons (C=C) at C-3 and C-8 resonated at 107.3 and 109.9 ppm, respectively. The observation of these characteristic signals supports the successful formation of compound **4**. The carbonyl carbons appeared in the range of 154.1–169.6 ppm, while the aromatic carbon resonances were distributed over the range of 120.3–141.5 ppm. In addition, HR-MS spectrum revealed that the mass of **4** is found at 228.0415 (Figure 4 and Figure 5).

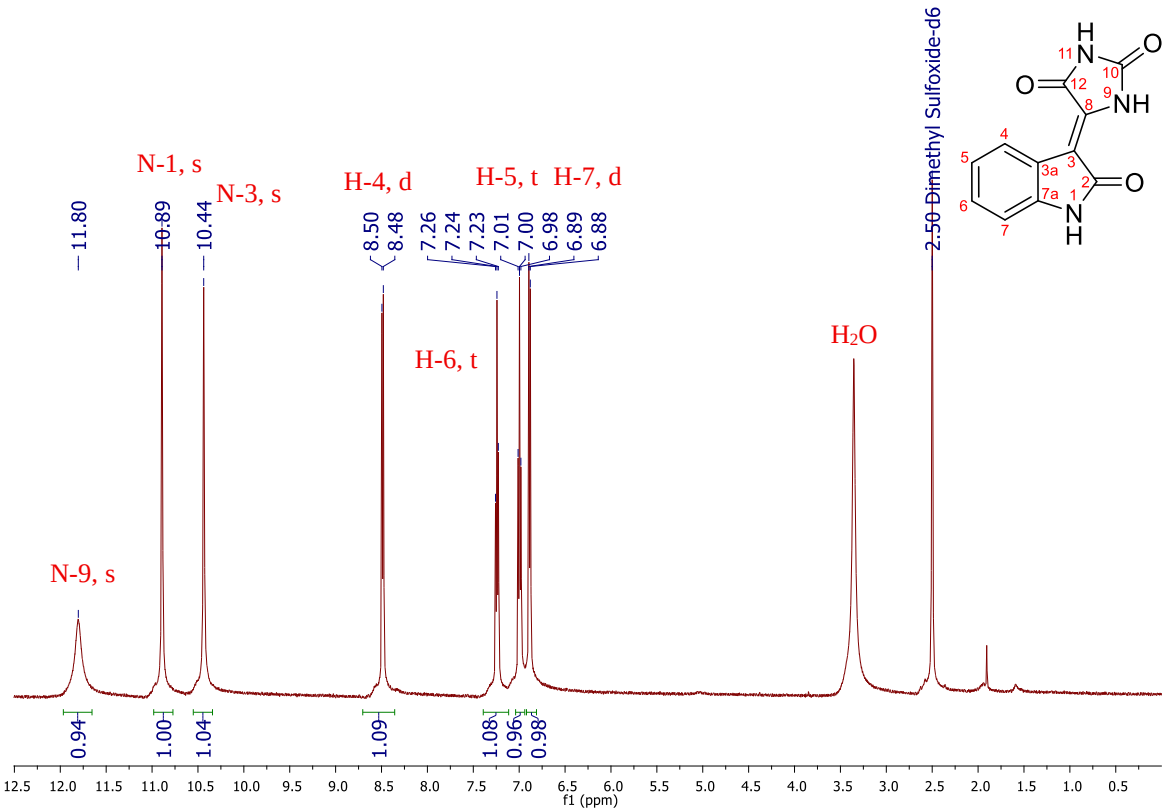

Figure 3. ^{1}H-NMR (500 MHz) of compound **4** in DMSO-d_6 (s = singlet, d = doublet, t = triplet).

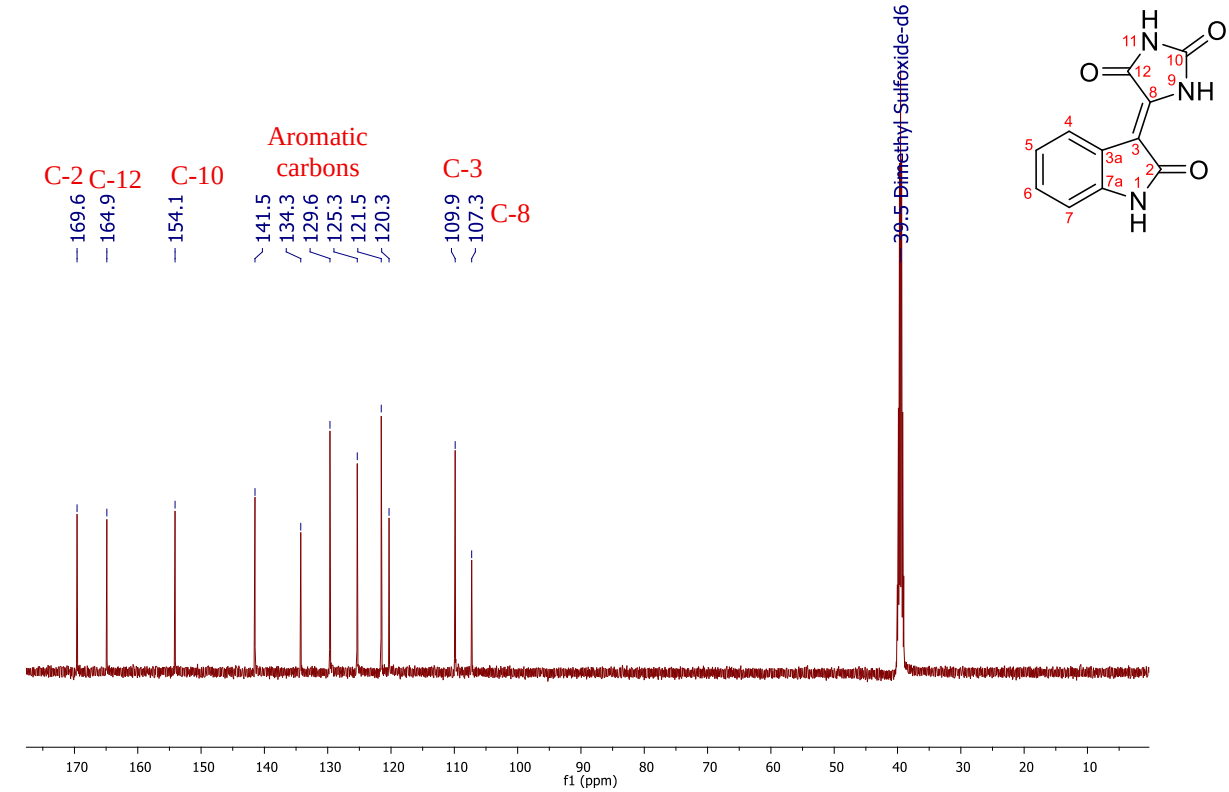

Figure 4. ^{13}C-NMR (125 MHz) of compound **4** in DMSO-d_6.

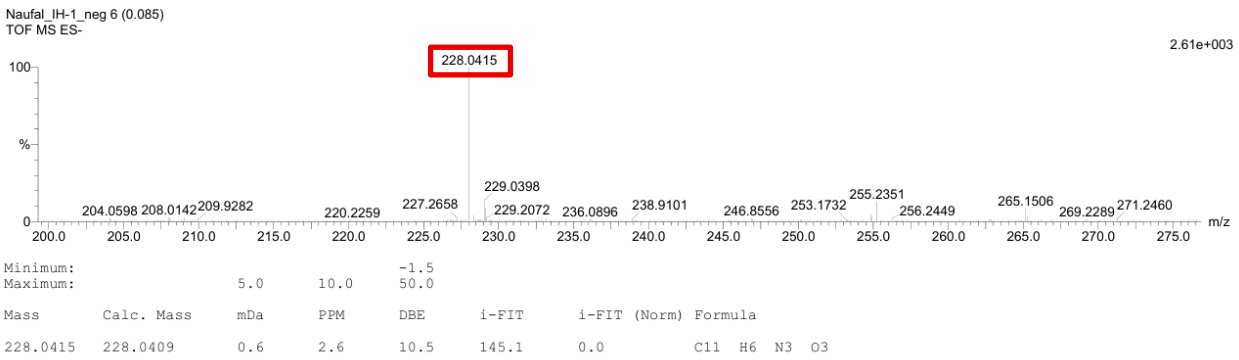

Figure 5. HR-TOF-MS of compound **4**.

The calculated frontier molecular orbital energies of compound **4** revealed a HOMO energy of −6.07 eV and a LUMO energy of −2.80 eV, resulting in a HOMO–LUMO energy gap of 3.27 eV (Figure 6). The moderate energy gap indicates a balance between electronic stability and chemical reactivity, while the relatively low LUMO energy suggests an appreciable electron-accepting capability of the molecule. Based on the frontier orbital energies, the ionization potential and electron affinity were estimated to be 6.07 and 2.80 eV, respectively. The calculated chemical hardness (η = 1.64 eV) and electronegativity (χ = 4.44 eV) indicate moderate resistance to electronic redistribution and a relatively strong tendency to attract electron density. The negative chemical potential (μ = −4.44 eV) is consistent with the electronic stability of compound **4**. Furthermore, the electrophilicity index (ω = 6.02 eV) indicates a pronounced tendency of compound **4** to accept electron density (Table 1). The HOMO is predominantly distributed over the π-conjugated framework, whereas the LUMO shows substantial contribution from the conjugated carbonyl-containing region. The spatial redistribution of electron density between these frontier orbitals further reflects the polarized electronic character of the isatin–hydantoin scaffold.

Table 1. Global reactivity descriptors of compound **4**.

Parameter (eV)	**Compound 4**
HOMO	-6.07
LUMO	-2.80
IP	6.07
EA	2.80
HLG	3.27
η	1.64
χ	4.44
μ	-4.44
ω	6.02

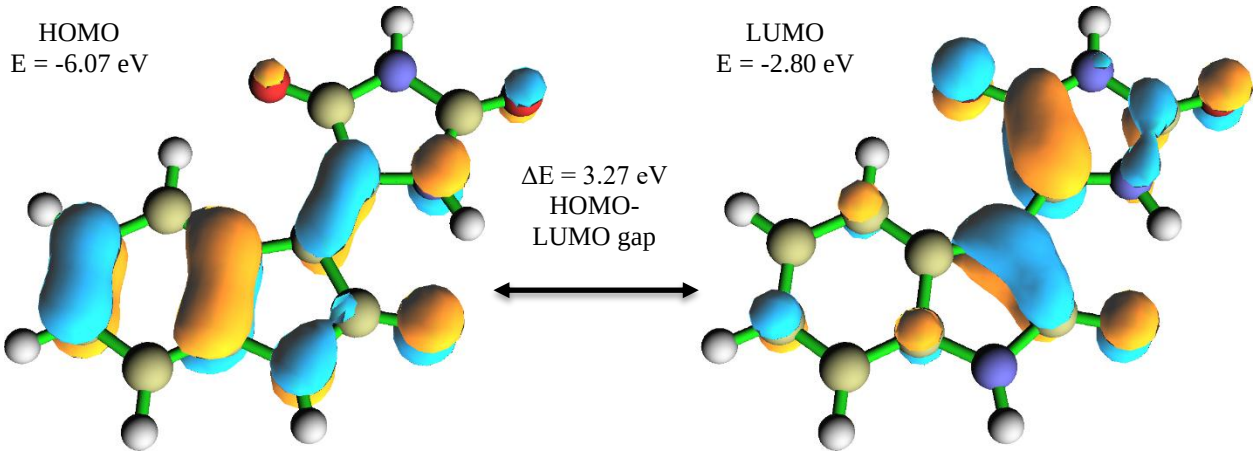

Figure 6. HOMO-LUMO visualization of compound **4**.

The electron localization function (ELF) and localized orbital locator (LOL) maps of compound **4** provide further insight into its electron-density distribution (Figure 7). The ELF map exhibits pronounced localization around the heteroatom centers, particularly the oxygen atoms, which can be attributed mainly to localized lone-pair electrons. High ELF values are also observed within the bonding regions, reflecting the covalent character of the molecular framework. In addition, the distribution of electron localization across the conjugated carbon framework indicates that the electron density is not restricted to individual bonds but is partially delocalized throughout the π-conjugated system. The LOL map shows a similar overall pattern, with enhanced orbital localization around heteroatoms and along the principal covalent bonds. The continuous localization features across the conjugated framework are consistent with π-electron delocalization between the aromatic and heterocyclic portions of compound **4**. Overall, the ELF and LOL analyses indicate the coexistence of localized lone-pair and bonding electron density with delocalized π-electron character, supporting the electronically conjugated nature of the isatin–hydantoin scaffold.

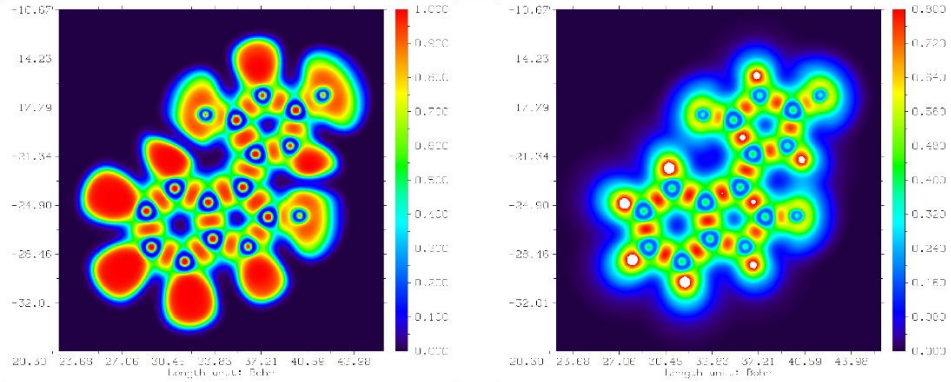

Figure 7. ELF and LOL visualization of compound **4** in 2D.

In the 1Q41 crystal structure, the ATP-binding site of GSK-3β is occupied by the co-crystallized ligand indirubin-3-monooxime. Therefore, the docking grid was centered on the position of the native ligand. Redocking of the co-crystallized ligand yielded an RMSD of approximately 0.4 Å, indicating only a minor deviation between the predicted and experimentally determined binding poses. As shown in Figure 8A, the native ligand establishes hydrogen-bond interactions with the hinge residues Val135 and Asp133. Similar hinge-binding interactions are also observed for the adenine moiety of the non-hydrolyzable ATP analogue adenyl imidodiphosphate (AMP-PNP) and for staurosporine, a potent GSK-3β inhibitor [19]. These conserved interactions highlight the importance of the hinge region in

the design of GSK-3β inhibitors. Compound **4** likewise forms hydrogen-bond interactions with Asp133 and Val135, mediated by its indole moiety. In contrast, the smaller hydantoin moiety of compound **4** provides weaker hydrophobic interactions with Thr138 compared with the native ligand (Figure 8B). The potential contribution of this difference in binding interactions to the inhibitory activity of compound **4** against GSK-3β remains to be evaluated experimentally.

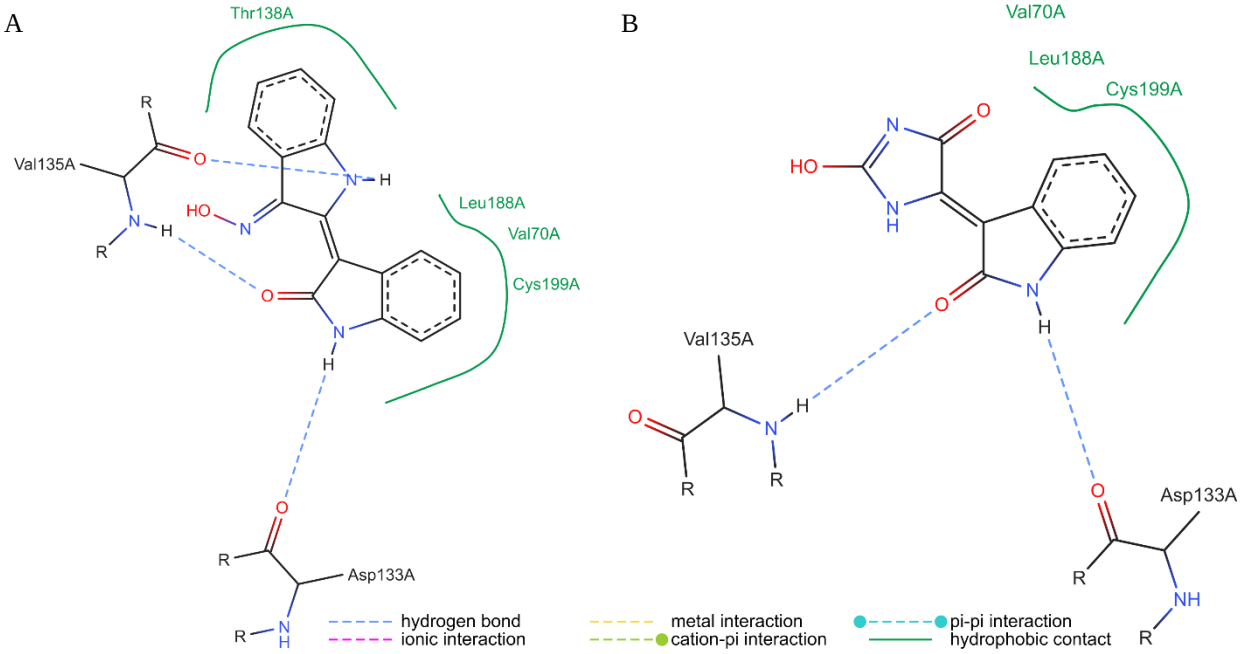

Figure 8. Two-dimensional interactions of indirubin-3-monooxime (A) and compound **4** (B).

CONCLUSION

Compound **4** was successfully synthesized via Knoevenagel condensation and fully characterized by NMR and HRMS. DFT analysis revealed a moderate HOMO–LUMO gap, and pronounced electrophilic character, while ELF and LOL maps supported a conjugated electronic structure with localized heteroatom contributions. Molecular docking indicated that compound **4** binds within the GSK-3β ATP site and reproduces key hinge interactions with Asp133 and Val135 through its indole moiety, although its hydantoin portion provides weaker hydrophobic contacts than the native ligand. Therefore, 5-(2-oxoindolin-3-ylidene)imidazolidine-2,4-dione (**4**) represents a viable lead scaffold for GSK-3β inhibition. Further synthetic derivatization and in vitro enzymatic assays are warranted to confirm its biological potential.

ACKNOWLEDGEMENT

The author would like to thank the Laboratory of Integrated Chemistry, Faculty of Mathematics and Natural Sciences, Institut Teknologi Bandung for providing the NMR and mass spectrometry facility.

REFERENCES

(1) Hu, Z.; Tu, Y.; Xia, Y.; Cheng, P.; Sun, W.; Shi, Y.; Guo, L.; He, H.; Xiong, C.; Chen, S.; Zhang, X. Rapid Identification and Verification of Indirubin-Containing Medicinal Plants. *Evidence-Based Complementary and Alternative Medicine* **2015**, *2015* (1), 484670. https://doi.org/10.1155/2015/484670

(2) Kurniawan, C. EKSTRAKSI INDIGO DARI DAUN STROBILANTHES CUSIA DAN KAJIAN PEMBENTUKAN KOMPLEKS DENGAN ION Ni2+. *Jurnal Kimia dan Kemasan* **2020**, *42*, 93–99.
(3) Qi-yue, Y.; Ting, Z.; Ya-nan, H.; Sheng-jie, H.; Xuan, D.; Li, H.; Chun-guang, X. From Natural Dye to Herbal Medicine: A Systematic Review of Chemical Constituents, Pharmacological Effects and Clinical Applications of Indigo Naturalis. *Chin Med* **2020**, *15* (1), 127. https://doi.org/10.1186/s13020-020-00406-x
(4) Klaas, S.; Vill, V.; Straske, F. Indirubin as a Red Hair Colourant from Indigofera Tinctoria L. *International Journal of Cosmetic Science* **2025**, *47* (5), 877–886. https://doi.org/10.1111/ics.13076
(5) Riniati; Widiastuti, E.; Marlina, A.; Taufiqurohim, T. Extraction Of Indigo Dye From Strobilanthes Cusia Leaves With Alkalization Process Using Sodium Hydroxide. *Jurnal Riset Kimia* **2026**, *17* (1), 133–147. https://doi.org/10.25077/jrk.v17i1.896
(6) Pardasani, R. T.; Pardasani, P.; Ojha, C. K.; Sherry, D.; Chaturvedi, V.; Sharma, I. Syntheses of Indigoid Dye Precursors and Bioactive Compounds Via Condensation of 1,2- and 1,4-Diones with Thiohydantoins. *Phosphorus, Sulfur, and Silicon and the Related Elements* **2002**, *177* (10), 2435–2443. https://doi.org/10.1080/10426500214123
(7) Blažević, T.; Heiss, E. H.; Atanasov, A. G.; Breuss, J. M.; Dirsch, V. M.; Uhrin, P. Indirubin and Indirubin Derivatives for Counteracting Proliferative Diseases. *Evidence-Based Complementary and Alternative Medicine* **2015**, *2015*, 1–12. https://doi.org/10.1155/2015/654098
(8) Aourz, N.; Serruys, A.-S. K.; Chabwine, J. N.; Balegamire, P. B.; Afrikanova, T.; Edrada-Ebel, R.; Grey, A. I.; Kamuhabwa, A. R.; Walrave, L.; Esguerra, C. V.; van Leuven, F.; de Witte, P. A. M.; Smolders, I.; Crawford, A. D. Identification of GSK-3 as a Potential Therapeutic Entry Point for Epilepsy. *ACS Chem. Neurosci.* **2018**, *10* (4), 1992–2003. https://doi.org/10.1021/acschemneuro.8b00281
(9) Yang, L.; Li, X.; Huang, W.; Rao, X.; Lai, Y. Pharmacological Properties of Indirubin and Its Derivatives. *Biomedicine & Pharmacotherapy* **2022**, *151*, 113112. https://doi.org/10.1016/j.biopha.2022.113112
(10) Hill, A. J.; Henze, H. R. CONDENSATION REACTIONS OF CYCLIC KETONES. I. THE ACTION OF ISATIN AND ISATIN ALPHA CHLORIDE UPON CERTAIN HYDANTOINS[1]. *Journal of the American Chemical Society* **1924**, *46* (12), 2806–2810. https://doi.org/10.1021/ja01677a030
(11) Chakrabarty, M.; Mukherjee, R.; Arima, S.; Harigaya, Y. Reaction of Isatins with Active Methylene Compounds on Neutral Alumina: Formation of Knoevenagel Condensates and Other Interesting Products. *HETEROCYCLES* **2009**, *78* (1), 139. https://doi.org/10.3987/com-08-11504
(12) Sun, M.; Ramsh, S. M.; Plotkin, V. N.; Solov'eva, S. Yu. Condensation of Pseudothiohydantoin with Substituted Isatins. *Russian Journal of General Chemistry* **2011**, *81* (9), 1886–1888. https://doi.org/10.1134/s1070363211090246
(13) Evdokimov, N. M.; Magedov, I. V.; McBrayer, D.; Kornienko, A. Isatin Derivatives with Activity against Apoptosis-Resistant Cancer Cells. *Bioorganic & Medicinal Chemistry Letters* **2016**, *26* (6), 1558–1560. https://doi.org/10.1016/j.bmcl.2016.02.015
(14) Hagemeister, M.; Hamilton, L.; Wandrey, N.; Hill, M.; Mounce, E.; Mosel, N.; Lytle, K.; Redinger, M.; Boley, J.; Fancher, N.; Haynes, A.; Fill, I.; Cole, P. A.; Hill, E.; Moxley, M. A.; Thomas, A. A. Evaluation of Rhodanine Indolinones as AANAT Inhibitors. *ChemMedChem* **2023**, *19* (1). https://doi.org/10.1002/cmdc.202300567
(15) Seliem, I. A. Design, Eco-Friendly Synthesis, and Molecular Docking Studies of Isatin Hybrids as Promising Therapeutic Agents (Anticancer, Anticholinesterase Inhibitor, α-Glucosidase

Inhibitor, and Anti-MRSA). *RSC Advances* **2025**, *15* (39), 32309–32327. https://doi.org/10.1039/d5ra04722f

(16) Neese, F. Software Update: The ORCA Program System, Version 6.0. *WIRES Comput. Molec. Sci.*, 2025, *15*, e70019. https://doi.org/10.1002/wcms.7019

(17) Pal, R.; Chattaraj, P. K. Chemical Reactivity from a Conceptual Density Functional Theory Perspective. *Journal of the Indian Chemical Society* **2021**, *98* (1), 100008. https://doi.org/10.1016/j.jics.2021.100008

(18) Lu, T. A Comprehensive Electron Wavefunction Analysis Toolbox for Chemists, Multiwfn. *The Journal of Chemical Physics* **2024**, *161* (8). https://doi.org/10.1063/5.0216272

(19) Bertrand, J. A.; Thieffine, S.; Vulpetti, A.; Cristiani, C.; Valsasina, B.; Knapp, S.; Kalisz, H. M.; Flocco, M. Structural Characterization of the GSK-3β Active Site Using Selective and Non-Selective ATP-Mimetic Inhibitors. *Journal of Molecular Biology* **2003**, *333* (2), 393–407. https://doi.org/10.1016/j.jmb.2003.08.031

(20) Forli, S.; Huey, R.; Pique, M. E.; Sanner, M. F.; Goodsell, D. S.; Olson, A. J. Computational Protein–Ligand Docking and Virtual Drug Screening with the AutoDock Suite. *Nature Protocols* **2016**, *11* (5), 905–919. https://doi.org/10.1038/nprot.2016.051

(21) Eberhardt, J.; Santos-Martins, D.; Tillack, A. F.; Forli, S. AutoDock Vina 1.2.0: New Docking Methods, Expanded Force Field, and Python Bindings. *J. Chem. Inf. Model.* **2021**, *61* (8), 3891–3898. https://doi.org/10.1021/acs.jcim.1c00203

(22) Schöning-Stierand, K.; Diedrich, K.; Ehrt, C.; Flachsenberg, F.; Graef, J.; Sieg, J.; Penner, P.; Poppinga, M.; Ungethüm, A.; Rarey, M. Proteins*Plus*: A Comprehensive Collection of Web-Based Molecular Modeling Tools. *Nucleic Acids Research* **2022**, *50* (W1), W611–W615. https://doi.org/10.1093/nar/gkac305